Composite Structures 289 (2022) 115455

Contents lists available at ScienceDirect

Composite Structures

journal homepage: www.elsevier.com/locate/compstruct

Structural Mechanics of cylindrical fish-cell zero Poisson's ratio metamaterials

Qing Qin, Iman Dayyani *, Phil Webb

Centre for Structures, Assembly and Intelligent Automation, Cranfield University, MK43 0AL, UK

ARTICLE INFO

Keywords:
Lattice Structures
Cylindrical Metamaterial
Zero Poisson's Ratio
Buckling
Modal analysis

ABSTRACT

In this paper, a novel cylindrical metamaterial exhibiting zero Poisson's ratio in two different directions is introduced. Detailed CAD modelling of a curved Fish-Cells necessary for numerical and experimental analysis are presented. High-fidelity finite element models are developed to assess the homogenisation studies of Poisson's ratio, Young's modulus and torsion behaviour, demonstrating the curvature effect and independency of the mechanical behaviour of cylindrical Fish-Cells metamaterial from tessellation numbers. Experimental analysis is performed to validate the zero Poisson's ratio, deformation and fracture mechanism discussed in numerical simulations. Moreover, buckling and modal behaviours of the cylindrical Fish-Cells metamaterials are studied and compared with equivalent shell models.

1. Introduction

Metamaterials are synthetic materials where their properties are designed to be unachievable with original constituent materials. Their microstructure is formed by unique shapes of unit cells with periodic arrangement to provide desired exotic behaviour. Rapid development of advanced manufacturing technologies has enabled the fabrication of complex structures in microscopic scales, which have attracted increasing attention to mechanical metamaterials such as: Poisson's ratio tailored metamaterials. Tuned Poisson's ratio mechanical metamaterials can possess negative, zero or positive values. Negative Poisson's ratio (NPR) metamaterials are the most widely studied type of mechanical metamaterials. They can provide superior energy absorption and high fracture resistance due to expansion of periodic unit cell geometry under compression [1,2]. Zero Poisson's Ratio (ZPR) metamaterials have received less attention in compare to NPR metamaterials, they expose no transverse displacements and undesired double curvatures under in-plane longitudinal loadings and out of plane bending moments [3]. This can lead to excellent characteristics for integration with complex geometries and boundary conditions, such as 2D planar morphing skins [4].

Gong et al. [5] have design a 2D star-shape cellular honeycomb structure based on analytical and numerical models, that could achieve ZPR behaviour in two orthogonal directions. They found that the mechanical properties such as stress and Young's modulus can be homogenised by tuning the aspect ratio of the unit cell with tessellations number fixed. Mizzi et al. [6] also manufactured a similar star-shaped 2D structure. They found that Poisson's ratio can reach negative to zero by tuning the angle and numbers of star horns. Grima et al. [7] presented a novel 'semi re-entrant honeycomb' that can achieve ZPR in one direction, followed by studying the mechanical behaviour of re-entrant and non-re-entrant honeycombs. Their research indicated Poisson's ratio can be neutralized by combine geometries with positive and negative Poisson's ratios. Yang et al. [8] designed a self-recovering structure with ZPR behaviour under large tensile strains. Their experiment and numerical results show that the structure can maintain ZPR behaviour at 40% strain.

In comparison to 2D ZPR skins, very few research articles might be found on 3D ZPR metamaterials. Some potential applications in morphing submarines with high fuel efficiency and reduced weight [9], soft robotics for works in narrow cylindrical spaces [10] and medical stents [11]. Moreover, Liu et al. [12] designed a 2D structure with isotropic negative Poisson's ratio under large tension and compared the deformation shape with its 3D form. However, they reported Poisson's ratio values near zero. They discussed that Poisson's ratio for 2D planar and 3D cylindrical structures with the identical unit cells and tessellation numbers have different values.

Despite very few research on 3D cylindrical ZPR metamaterials, there exist some investigations focused on cylindrical structures with Negative Poisson's ratio. Gao et al. [13] presented an analytical method

* Corresponding author.
E-mail addresses: Iman.Dayyani@gmail.com, I.Dayyani@cranfield.ac.uk (I. Dayyani).

https://doi.org/10.1016/j.compstruct.2022.115455
Received 30 July 2021; Received in revised form 31 January 2022; Accepted 3 March 2022
Available online 12 March 2022
0263-8223/© 2022 The Authors. Published by Elsevier Ltd. This is an open access article under the CC BY license (http://creativecommons.org/licenses/by/4.0/).

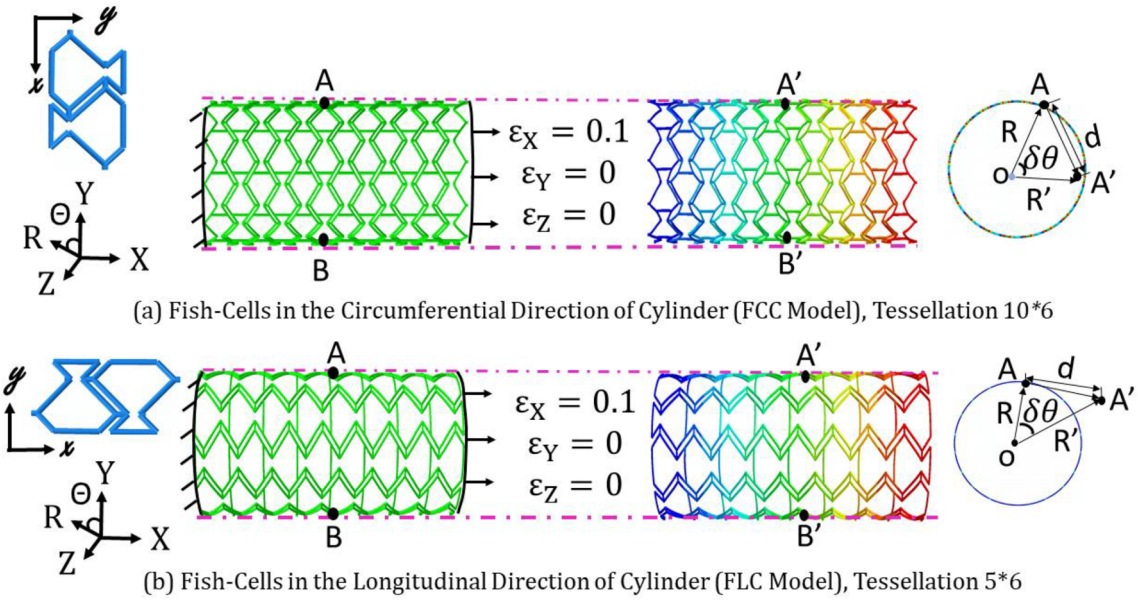

Fig. 1. Zero Poisson ratio simulations of cylindrical Fish-Cells metamaterials with two different arrangements.

to analyse a cylindrical structure with truss-like extruded pattern exhibiting high strength and Poisson's ratio of minus seven. Chiral structure has unique rotation mechanism to maintain the negative Poisson's ratio under large tension. The cylinder provides superior advantages over traditional hexagonal structures and lattice structure, in such structure, the in-plane stress and compressive strength are partially decoupled between cylinder and ligaments during the rotation deformation [14]. Not only the unit cell has rotation characteristics, tension–torsion coupling was observed in chiral cylindrical metamaterials under axial loading [15–18]. Frenzel et al. [18] performed an experiment on 3D chrial cubic structure, increasing the unit cell size and tessellation numbers can efficiently minimize the torsion of the structure. Moreover, Ma et al. [19] manufactured chiral cylinders formed by nylon and aluminium. Where torsion mechanism was independent from the constitutive materials. They showed the deformation mechanism such as local torsion of the unit cell and tessellation numbers have significant effect on global torsion which can be tuned by changing the aspect ratio of the cylinder.

Deformation mechanism of cylindrical metamaterials maybe similar to some lattice cylinder structure. Lattice structures like cellular metamaterials contains notches and well organised beam elements. They can be lightweight with high strength and specific stiffness [20–22]. Material failure, axisymmetric global buckling and local buckling are considered as three failure criteria [23]. It is assumed structure failure when one of the criteria satisfied. The study of Zhang et al. [24] indicated that cross-section shape of different types of lattice cylinders under buckling loading is affected by beam cross-section shapes and loading directions. Their research showed the effect of relative density i.e. the tessellation numbers on the elastic buckling load. Lattice structure with higher non periodical order show lower stiffness, strength and brittleness [21]. Nguyen and Cong et al. [25,26]present nonlinear dynamic response and vibration for auxetic honeycombs in planar and cylindrical form. Li et al. [27] analysed the free vibration on a cylindrical carbon fibre reinforced lattice sandwich structure with experimental and computational methods. They found that the free vibration was mainly located at the cross-sectional plane. Also, a free vibration of a cantilever composite lattice cylindrical shell was studied by Lopatin et al. [28] which revealed the effect of the angle for orientation of unidirectional helical ribs on the magnitude of fundamental frequency.

The mechanical behaviour of cylindrical ZPR metamaterials is not studied by literature comprehensively. In this work, a novel cylindrical metamaterial with ZPR behaviour formed by Fish-Cells architecture is introduced. The method of generating the complex geometry in CAD is explained in detail. Experimental and numerical analysis are performed to demonstrate the ZPR behaviour of a homogenised cylindrical tessellation. Moreover, linear buckling and vibration behaviours of the cylindrical Fish-Cells metamaterials are studied and compared with equivalent shell models.

2. Cylindrical Fish-Cells metamaterial architecture

Fish-Cells was introduced recently as a new metamaterial with ZPR and compliance in two planar directions by Naghavi Zadeh et al. [29]. The periodic unit cell is comprised of two Fish-Cells in opposite directions to demonstrate zero Poisson's ratio. The head of the fish is a hexagon shape exhibiting positive Poisson's ratio while the tail part is auxetic re-entrant structure with negative Poisson's ratio.

For the first time in literature, the cylindrical Fish-Cells ZPR metamaterial is proposed in this paper with two different arrangements of unit cells concerning the longitudinal axis of a cylinder, as shown in Fig. 1. Fig. 1(a) shows arrangement of Fish-Cells in Circumferential direction of Cylinder (FCC model), where local "y" axis of unit cell is aligned with the global circumferential direction of a cylinder. Fig. 1(b) shows arrangement of Fish cells in Longitudinal direction of Cylinder (FLC model), where local "y" axis of unit cell is aligned with global longitudinal axis of a cylinder.

Dimensions for the unit cell of cylindrical Fish-Cells can be defined by seven parameters as presented in Appendix A. These parameters refer to base member length$B$, inclined rib's horizontal length$b$, inclined rib's vertical length$h$, unit cell's height$H$, the connector's length$C$, the uniform thickness of each member t and radius of cylinder$R$. The length of the cylinder can be calculated based on tessellation numbers. Tessellation numbers for numerical and experimental models are presenting in "m*n" format, where "m" presents the unit cell numbers in the circumferential direction and "n" shows unit cell numbers in the axial direction of the cylinder. For example, Fig. 1(a) demonstrates the FCC model with tessellation 10*6, i.e., 10 unit cells in the circumferential direction and six unit cells in the axial direction of the cylinder. Similarly, Fig. 1(b) demonstrates the FLC model with tessellation 5*8, i.e. Five unit cells in circumferential direction and eight unit cells in the axial direction of the cylinder.

It must be mentioned that the complex geometries of cylindrical Fish-

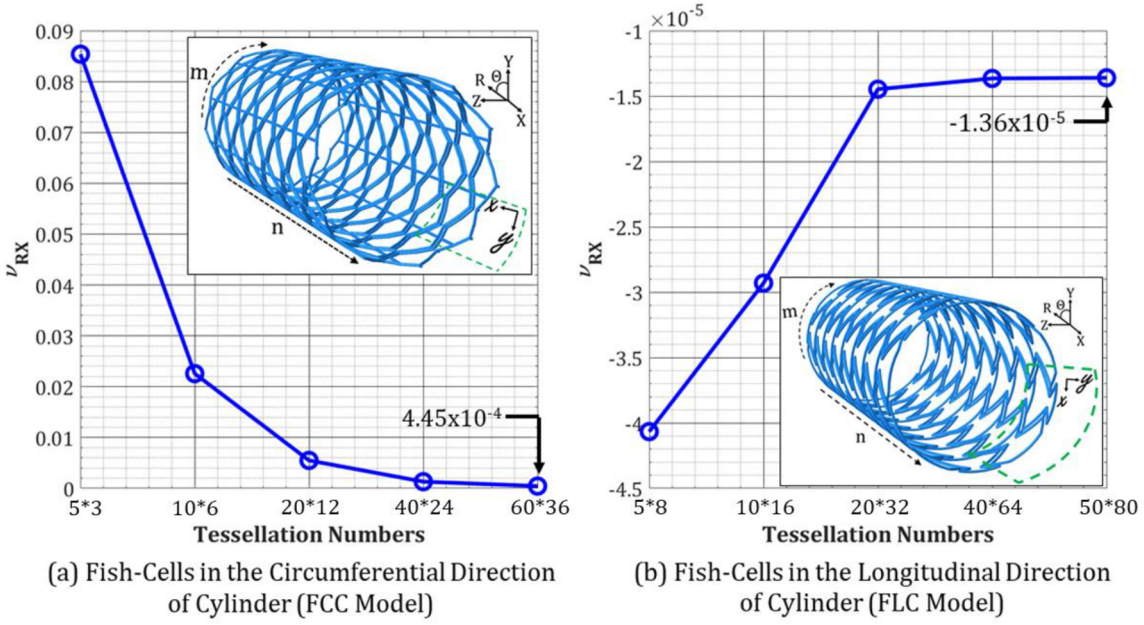

(a) Fish-Cells in the Circumferential Direction of Cylinder (FCC Model)

(b) Fish-Cells in the Longitudinal Direction of Cylinder (FLC Model)

Fig. 2. Homogenised trend of Poisson's Ratio ν_{RX} with various tessellation numbers for Cylindrical Zero Poisson's Ratio Fish-Cells Metamaterials.

Cells structures make the Computer-Aided Design (CAD) modelling very delicate and time-consuming. For example, the aspect ratio of the unit cell changes due to normal projection of a 2D planar unit cell on a curved surface of cylinder. Therefore, a unit cell is created directly on the curved surface of a cylinder using "support" function in CATIA V5, ensuring high fidelity model dimensions. Moreover, the dimension of the geometry must be represented accurately by at least seven decimal places to assure successful assembly of model and accurate analysis.

Appendix A presents the unit cell and its geometric parameters, as well as their values for various homogenization studies. The ratio of the dimension is identical to the fish cell created by Naghavi Zadeh et al. [29]. In order to study tessellation effects, the size of the cylinder remained constant, but the size of the unit cell varied. For FCC model, the tessellation on circumferential direction (m) is selected firstly, then the radius of the cylinder can be calculated as$R = \frac{m^{*}L_{UC-axial}}{2\pi}$, where $L_{UC-axial}$ is the length of the unit cell on axial direction. The cylinder length is set to L = 6R in order to consider long aspect ratio. Finally, the tessellation numbers on longitudinal direction (n) can be calculated as $n = \frac{L}{L_{UC-longitudinal}}$, where $L_{UC-longitudinal}$ is the unit cell length in longitudinal direction. For FLC model, the dimension of the unit cell and the tessellations on circumferential direction (m) are identical to FCC model, in addition the radius of the cylinder (R) can be found by $R = \frac{mL_{UC-longitudinal}}{2\pi}$. While the length of the cylinder remained as L = 6R, the tessellation numbers on longitudinal direction (n) can be found as $n = \frac{L}{L_{UC-axial}}$. It must be mentioned that the dimensions of cylinder i.e. the cylinder radius (R) and length (L) are fixed in both FCC and FLC models for Poisson's ratio study, however eight different dimension values are considered in Young's modulus study.

3. Zero Poisson ratio cylindrical fish-cells, concept validation

In Continuum Mechanics, six Poisson's ratios can be disused for cylindrical coordinate system known as:$\nu_{X\theta}$,$\nu_{\theta X}$;ν_{XR}, ν_{RX} ; $\nu_{R\theta}$ and $\nu_{\theta R}$. However, considering morphing applications where actuation will be in longitudinal directions of cylinder, two Poisson's ratios of $\nu_{\theta X}$ and ν_{RX} are critical for integration perspectives. Poisson's ratio ν_{RX} shows the negative ratio of radius change to longitudinal displacements of the cylinder, i.e.$\nu_{RX} = -\frac{\varepsilon_{RR}}{\varepsilon_{XX}}$, where ε_R is the strain in radios direction, i.e.$\varepsilon_{RR} = \frac{\partial u_R}{\partial R}$, and ε_x is the longitudinal strain, i.e.$\varepsilon_{XX} = \frac{\partial u_X}{\partial_x}$. In addition,

Table 1
Homogenised Trend of Poisson's Ratio $\nu_{\theta X}$ with Various tessellation numbers for Cylindrical Zero Poisson's Ratio Fish-Cells Metamaterials.

Model FCC	5*3	10*6	20*12	40*24	60*36
$\nu_{\theta X}$	8.54×10^{-2}	5.47×10^{-2}	5.38×10^{-3}	1.26×10^{-3}	4.11×10^{-4}
Model FLC	5*8	10*16	20*32	40*64	50*80
$\nu_{\theta X}$	-4.05×10^{-5}	-2.91×10^{-5}	-1.45×10^{-5}	-1.37×10^{-5}	-1.07×10^{-5}

Poisson's ratio $\nu_{\theta X}$ indicates the negative ratio of torsion to stretch of cylinder in longitudinal direction, i.e.$\nu_{\theta X} = -\frac{\varepsilon_{\theta\theta}}{\varepsilon_{XX}}$, where ε_θ is torsional strain in circumferential direction of cylinder, i.e $\varepsilon_{\theta\theta} = \frac{u_R}{R} + \frac{1}{R}\frac{\partial u_\theta}{\partial \theta}$..

To study these Poisson's ratios and mechanical behaviour of the cylindrical metamaterial, numerical simulations are used to analyse the ZPR concept. Simulations are carried out using Abaqus V6.18 with Nylon PA2200 material properties of Poisson's ratio$\nu = 0.4$, Young's modulus $E = 1130$ MPa and density $\rho = 930$ kg/m^3. Boundary conditions for FCC and FLC models are presented in Fig. 1, where left ends of the models are constrained with all degrees of freedom. The right ends of the models allow moving only along the longitudinal X-direction of cylinder with strains of$\varepsilon_X = 0.1$. The models are simulated without nonlinear effects with three node quadratic beam elements B32 with circular cross-sections. Mesh convergence study is performed with minimum global mesh size of 0.5 mm to ensure accurate mesh quality. It must be mentioned tessellation numbers are limited by mesh time; for instance, FCC model 60*36 and FLC model 50*80 require four and seven hours to mesh with a high-performance computer.

Calculating ZPR behaviour of numerical models, arbitrary diameter ''AB'' at the middle of cylindrical metamaterial is considered, as shown in Fig. 1. Fig. 1 shows negligible displacement in diameter ''AB'', when both models are loaded in the longitudinal directions, indicating close to zero values of ν_{RX}. Regarding potential torsion-extension coupling shown in Fig. 1, angle of torsion difference $\delta\theta$ may be considered as:$\delta\theta = \mathrm{Cos}^{-1}\left(\frac{R^2 - R'^2 - d^2}{2RR'}\right)$, where $\vec{R}$ and $\vec{R'}$ are position vectors in original and

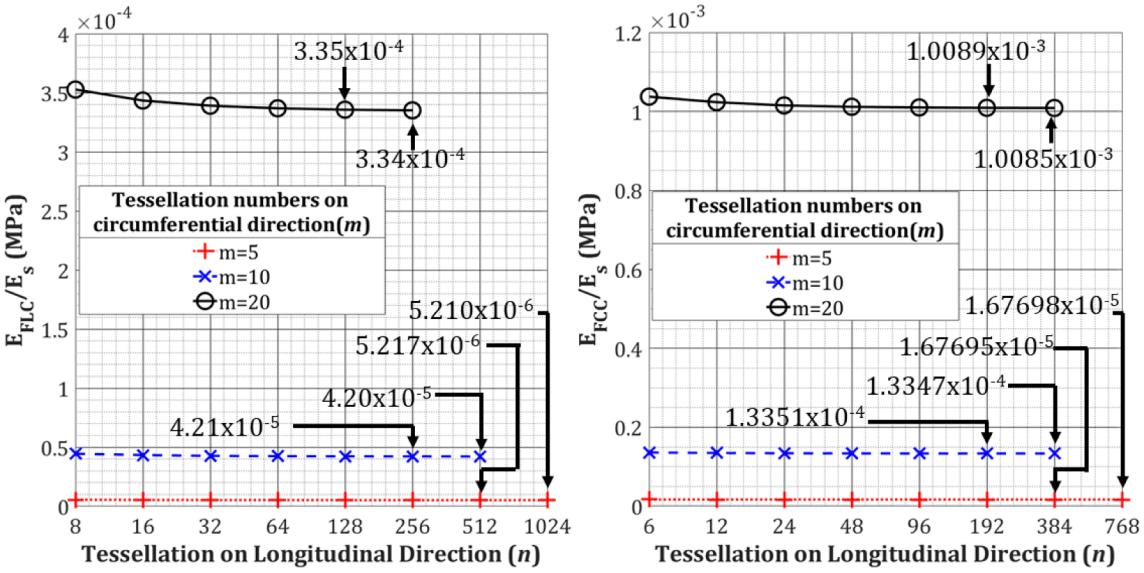

(a) Fish-Cells in the Longitudinal Direction of Cylinder (FLC Model)

(b) Fish-Cells in the Circumferential Direction of Cylinder (FCC Model)

Fig. 3. Effective Young's modulus of cylindrical Fish-Cells metamaterials with tessellation numbers on Longitudinal and Circumferential direction of the cylinder.

deformed configurations and $\vec{d}$ is the displacement vector as $\vec{d} = \vec{R}' - \vec{R}$. Detailed results demonstrating homogenised ZPR for these Poisson ratios are illustrated in Fig. 2 and Table 1 based on models with different tessellations presented in Appendix A.

3.1. Homogenization studies of Poisson ratios

The ratio of unit cell size to metamaterial dimension, load and boundary conditions effects has significant influence on the structural behaviour of metamaterials. Thus, it is necessary to perform homogenization study with different size ratios to introduce tessellation numbers demonstrating a behaviour convergence independent from these effects. As presented in Appendix A, different tessellation numbers of 5*3, 10*6, 20*12, 40*24 and 60*36 are considered for analysis of FCC model. In addition, tessellations of 5*8, 10*16, 20*32, 40*64 and 50*80 are used for investigation of FLC model. It should be mentioned that dimensions of cylinders in both models are constant with length to diameter ratio greater than three, avoiding short cylinders geometries. Thus, dimensions of unite cell change as a function of tessellation numbers as presented in Appendix A. Boundary conditions and imposed displacements are identical to what described in Fig. 1. Trend of Poisson's ratio ν_{RX} for different tessellations of FCC and FLC models are illustrated in Fig. 2.

Fig. 2(a) shows decreasing trend of positive Poisson's ratio ν_{RX} by increase of tessellation numbers in FCC model. The trend converges to value of $\nu_{RX} = 4.45\times10^{-4}$ at tessellation 60*36. However, Fig. 2(b) demonstrate an increasing negative Poisson's ratio ν_{RX} by increase of tessellation numbers in FLC model. This trend converges to value of $\nu_{RX} = -1.36 \times 10^{-5}$ at tessellation 40*64. Also Fig. 2 concludes that Cylindrical Fish-Cells metamaterial show zero Poisson ratio behaviour independent of unit cell propagation. The results show that the values of ν_{RX} in FLC model is much lower than FCC model. Unlike 2D Fish-Cells skin [29], cylindrical Fish-Cells metamaterial requires larger tessellation numbers to reach homogeneity.

Similarly, Poisson's ratio $\nu_{\theta X}$ shows convergence and homogenised trends comparing to Poisson's ratioν_{RX}. For calculation of$\nu_{\theta X}$, the assumption $\theta = 2\pi$ is made in$\varepsilon_{\theta\theta} = \frac{u_R}{R} + \frac{1}{R}\frac{\partial u_\theta}{\partial\theta}$. For model FCC $\nu_{\theta X}$ decreases as tessellation numbers increase, the minimum value is at 60*36 with $\nu_{\theta X} = 4.11 \times 10^{-4}$ rad. Model FLC have a tension–torsion coupled feature, the maximum value of $\nu_{\theta X}$ is -1.07×10^{-5} rad for tessellation number 50*80. The data for $\nu_{\theta X}$ of both models are listed in Table 1.

3.2. Homogenization studies of Young modulus

Effective Young's modulus of Fish-Cells metamaterial in the axial direction of cylinder, i.e. E_{XX} can be defined as:$E_{XX} = \frac{\sigma_X}{\varepsilon_X} = \frac{LF_X}{2\pi Rt\delta_X}$, where$F_X$,$\delta_X$,$L$, R and t refer to reaction force, imposed displacement, length and radius of cylinder as well as elements thickness, respectively.

Calculating effective Young's modulus, three categories with fixed numbers of tessellation in the circumferential direction i.e. $(m = 5, 10, 20)$ are considered for both FCC and FLC models. The length of cylinders is dependant to tessellation number in the longitudinal direction$n$, which maybe represented as$n = \frac{L}{L_{UC-axial}}$, where $L_{UC-axial}$ is length of unit cell in the axial direction of cylinder. Size of unit cell parameters are listed in Appendix A.

Effective Young's modulus results are illustrated in Fig. 3(a) and (b) show the Young's modulus of Fish-Cells metamaterial is dramatically smaller than original constructing material. Furthermore, Young's modulus of both models shows homogenised behaviour when tessellation numbers on circumferential direction(m) is fixed but tessellation numbers on longitudinal directions(n) increases. However, when tessellation on longitudinal direction (n) is fixed, Young's modulus rises with increase of tessellation numbers on circumferential direction (m). Due to the excellent zero Poisson's ratio behaviour and the low stiffness, the cylindrical metamaterials can be applied in applications such as medical stents where low stiffness is required.

4. Experimental analysis

4.1. Manufacturing

The complexity of cylindrical Fish-Cells with homogenised tessellation and minimised boundary condition effects makes their manufacturing very expensive and complicated. Selective Laser Sintering (SLS) technology is applied for 3D printing of the material with immensely low tolerance and fine surface finish. The main limitation of additive manufacturing is the minimum achievable thickness of the unit cell ribs. Moreover, Molten Polymer Deposition (MPD) may not be

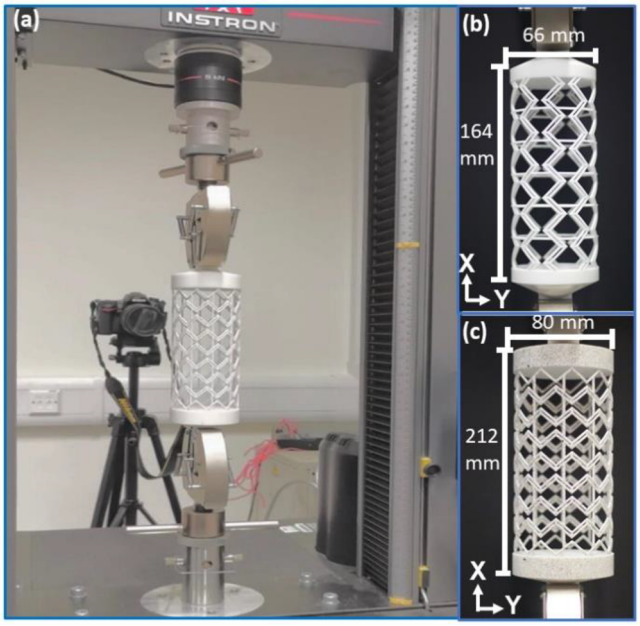

Fig. 4. Experimental set up with Digital Single Lens Reflex (DSLR) camera and 3D printed models. (a) experimental apparatus, (b) Fish-Cells in the Longitudinal direction of Cylinder (FLC model), (c) Fish-Cells in Circumferential direction of the Cylinder (FCC model).

Table 2
Material properties of constructing material Nylon PA2200 [29].

Material Elasticity	
Young's Modulus (E)	1130 MPa
Poisson's ratio (ν)	0.4
Material Plasticity	
Yield Stress (MPa)	Plastic Strain
14.0	0.0000
34.1	0.0025
42.7	0.0500
46.7	0.0750
49.0	0.1000
50.5	0.1250
51.3	0.1500
51.6	0.1750

suitable for the Cylindrical Fish-Cell structure, due to massive numbers of support needed to generate the structure, causing coarse finish and uneven thickness. Considering these limitations as well as constraint on tensile test area size, two samples of FLC model with tessellation 5*6 and FCC model with 10*4 are manufactured as illustrated in Fig. 4 with corresponding dimensions presented in Appendix A.

4.2. Material characteristics of Nylon PA2200

The material properties of the constructing material Nylon PA2200 needs to be investigated in order to validate the numerical models. For this purpose, five 3D printed specimens were also tested by simple tensile experiment to assess the mechanical properties. The average material properties for PA2200 from the tensile test are listed in Table 2.

4.3. Structural tests

The Poisson's ratio and the stiffness of two samples are tested by tensile experiments. Grippers are designed as rigid parts on cylinders ends for the installation on tensile machine to replicate the boundary conditions shown in Fig. 1. Digital Single Lens Reflex (DSLR) camera Nikon D7000 is using to capture changes of the structure at every five seconds to measure axial displacements and diameter deformations for calculation of Poisson's ratios. It should be mentioned that unlike 2D planar Fish-Cells [29] digital image correlation technique is not suitable due to the curvature of the cylinder and very small thickness of ribs elements. The lens of DSLR camera is placed horizontally to the middle of the cylinder to ensure the ratio of the length and pixels are correct. The axial tension is applied at a displacement rate of 2 mm/s. Poisson's ratios are measured based on images taken by DSLR camera, while Force-Displacement directly fulfilled by tensile machine. The change of diameter is calculated and collected based on the pixel in 'Plot Digitiser' software, where the ratio between pixel and the length is calculated.

5. Results and discussion

5.1. Poisson's ratio validations

A Poisson's ratio validation study between experiment and numerical models is presented in this section to prove the reliability of numerical models. 3D continuum quadratic solid elements, known as C3D10 are used for numerical analysis in ABAQUS. Mesh convergence studies are performed and a fine mesh with a global size of 0.65 mm is used for discretization, as shown in Fig. 5(a). Position of points ''A'' and ''B'' in experimental results are calculated by use of ''Plot Digitizer'' software, which converts the pixel of the experimental images into mathematical coordinates.

Fig. 5(b) shows Poisson's ratio as function of strain for both FCC and FLC models. The experimental and numerical results demonstrate a good correlation for Poisson's ratio values. The maximum error between simulation and experiments in FLC and FCC models are about 10.4% and 5.6% at strains 0.1320 and 0.0277, respectively. The main reason of higher error in FLC model is measuring method limitation as the deformation of the experiment sample is recorded by image processed in 'plot digitizer' software. This requires selection of the measuring points manually, where the accuracy of the results depends on the complexity of the geometry and quality of the image. FLC Model has a smaller poison ration compared to FCC model, making it more sensitive to measure the displacement in Plot digitizer, leading to more error between FLC experiment and FEA results compared to FCC model.

Fig. 5(b) shows that the positive Poisson's ratio of FLC model is increasing steadily as the tensile strain increases. FCC model also demonstrate a positive Poisson's ratio behaviour, but with oscillated descending trend. The FCC Poisson's ratio decreases from $\nu_{RX} = 0.208$ to $\nu_{RX} = 0.197$ within the strain range 0.01 to 0.02, then keep increasing until $\nu_{RX} = 0.205$ with strain 0.055, finally it reduces to $\nu_{RX} = 0.185$ at failure strain of 0.09.

The oscillated trend of FCC model can be investigated in three strain ranges. The decreasing trends of FCC Poisson's ratio in strain range (0.01–0.02) and strain range (0.055–0.09) are due to the out of plane bending of the Fish base elements. The increasing trend of FCC Poisson's ratio in 2nd strain range of (0.02–0.055) is due to slight rotations of the bended Fish base elements along the cylinder axis direction. The decreasing and increasing positive Poisson's ratio trends imply that the cylindrical structure is showing resistance and compliance to reduce its diameter, respectively. As expected, the values of Poisson's ratio are different in simulations with solid elements and beam elements [29,30]. The Poisson's ratio from solid elements can get closer to those predicted with beam elements by reducing the joint thickness of the unit cells [27].

5.2. Deformation and fracture mechanism validations

The deformation and fracture mechanism of cylindrical Fish-Cells metamaterials are compared between numerical and experimental models to reveal the reliability of numerical simulations in detailed study of the structures. The experimental and simulation models are using identical data for maximum displacement and solid elements discretization as mentioned in Section 5.1. Fig. 6 displays similar

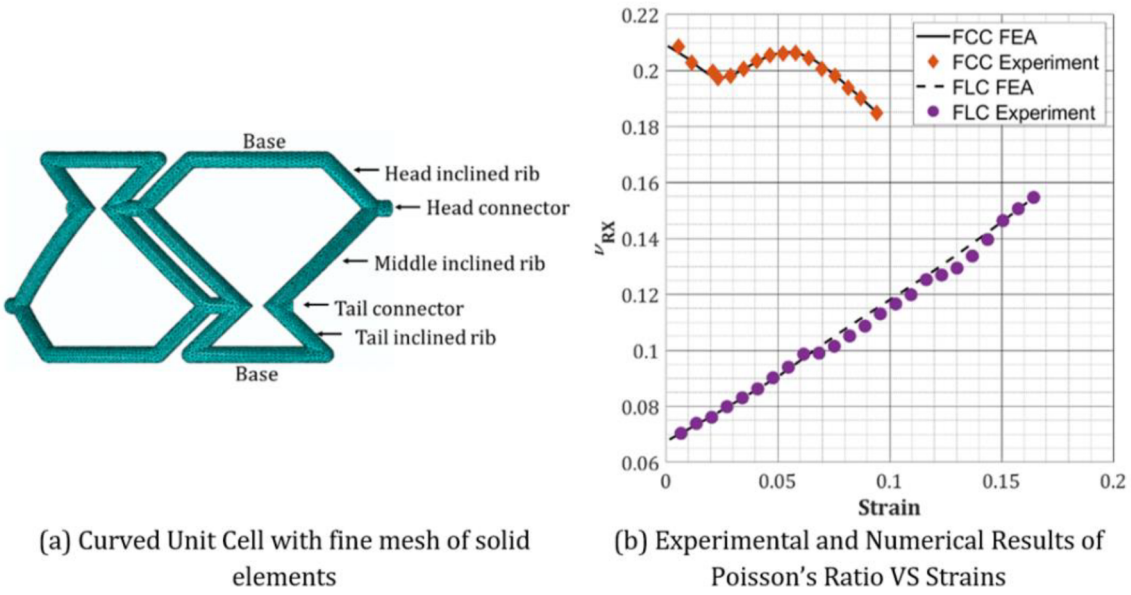

(a) Curved Unit Cell with fine mesh of solid elements

(b) Experimental and Numerical Results of Poisson's Ratio VS Strains

Fig. 5. Poisson's ratio behaviour as a function of tensile strain in model Fish-Cells in the Circumferential direction of Cylinder (FCC) and Fish-Cells in the Longitudinal direction of the Cylinder (FLC model).

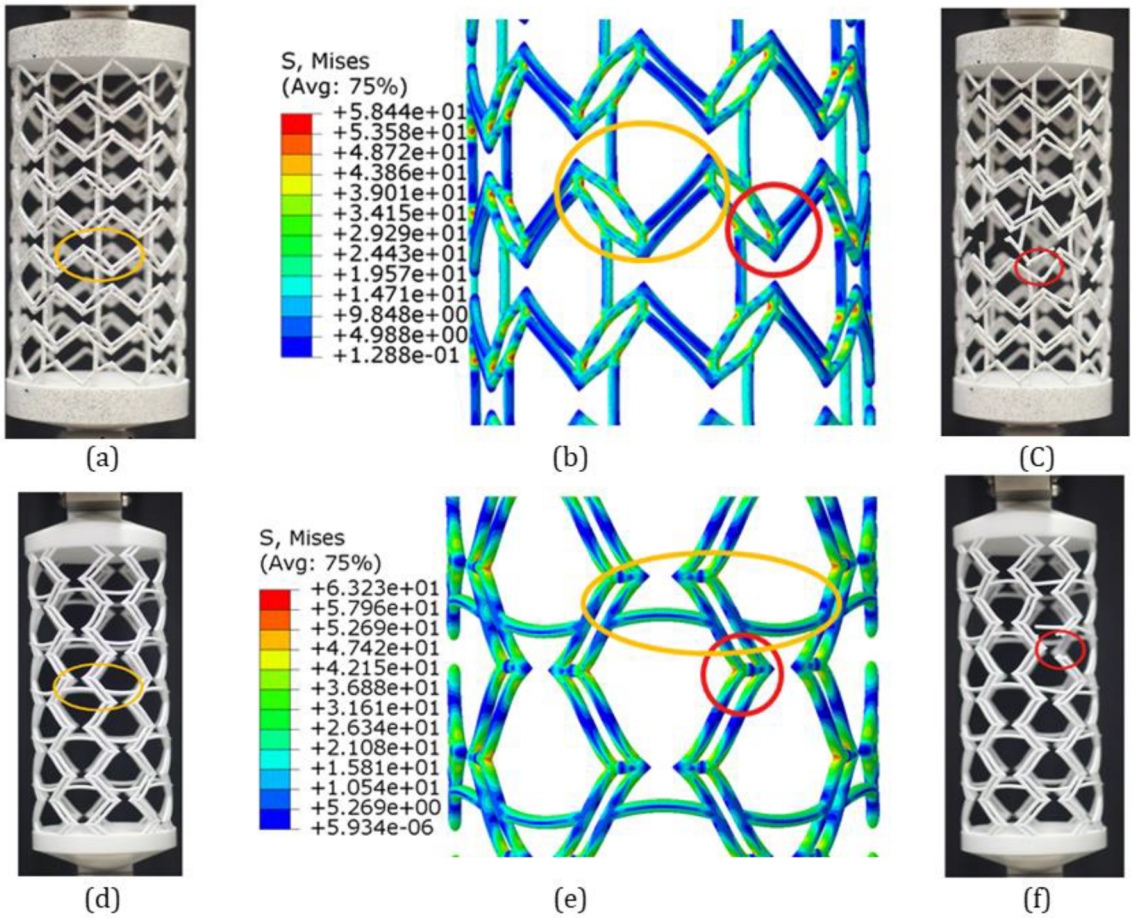

Fig. 6. Deformation and Fracture Mechanism of Fish-Cells in Circumferential direction of Cylinder (FCC Model) and Fish-Cell in Longitudinal direction of Cylinder (FLC Model) in simulation and experiment, (a) Experimental deformation mechanism of FCC model, (b) Numerical deformation mechanism of FCC model, (c) experimental fracture mechanism of FCC model, (d) experimental deformation mechanism of FLC model (e) numerical deformation mechanism of FLC model, (f) experimental fracture mechanism of FLC model.

Table 3
Buckling load and mode shapes for Fish-Cell in Circumferential Direction of the Cylinder (FCC model).

Tessellation	Critical buckling load (N)	Normalise critical load to weight	Buckling mode shape	Bending of cylinder axis	Cylinder rotation (degree)	Cross section change at middle
5*3	1.23	19.10	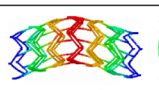	Yes	0	No change
10*6	8.97	69.53	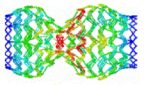	No	0.06	Peanut shape
20*12	45.01	174.46	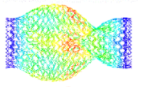	No	0.05	Peanut shape
40*24	152.36	295.27	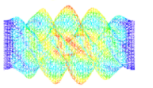	No	0.02	Three-pointed star
80*48	591.56	574.33	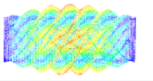	No	0.02	Five-Pointed Starfish

fracture locations with max stress as well as identical deformation mechanism in experiments and simulations. Also, the fracture mechanism study is constructive material dependant. Further research might be performed with metallic, composites and elastomer materials. This is beyond the scope of this paper as the focus is only on metamaterial architecture.

A typical deformation behaviour for FCC model is highlighted by yellow circles on both experimental and numerical models shown in Fig. 6 (a) and (b). The gap between the inclined ribs connected to fish cell bases i.e. head and tail inclined ribs as shown in Fig. 6 (a) increases as tensile strain increase in both models. This is due to the tension applied on the connectors which rotates the head and tail inclined ribs. Meanwhile, the fish cell bases also pull the inclined ribs, resulting in the increase of the gap between the head and tail inclined ribs. On the other hand, the gap between inclined ribs at the middle of the fish cell decreases as tensile displacement increases. Furthermore, the miss alignment of fish cell bases is observed in both simulation and experiment, indicating shear due to torsions between rings of Fish-Cells. With regards to fracture mechanism, the red circles shown in both experiment and simulation in Fig. 6 (b) and (c) highlight the first local failure with stress value of 58.4 MPa. This is because all joints almost reach identical maximum stress before initiation of the first local failure, but the force does not distribute evenly on the cylinder surface after the first crack initiation, leading to spine line fracture pattern.

Deformation characteristics of FLC model from experiment and simulation perspectives are illustrated by yellow circles in Fig. 6 (d) and (e). The wave shape of unit cells is due to compression of Fish-Cell bases connected to inclined ribs. This is because, the Fish head, i.e. the hexagon shape with positive Poisson's ratio is shrinking while the Fish tail i.e. the re-entrant shape with negative Poisson's ratio is expanding due to tension [29], which results in compression of Fish-Cell bases. Therefore, one Fish-Cell base element periodically bends slightly outward of cylinder, while the other bends inward, resulting in negligible increase and decrease of cylinder cross section. With regards to fracture mechanism, the locations of maximum stress with value of 63.2Mpa and first local failure are the joints of the inclined ribs at the middle of the Fish-Cell. The re d circles shown in both experiment and simulation in Fig. 6 (f) and (e) highlights similar locations.

The fracture mechanisms of FCC and FLC models are very different as they are formed with identical unit cells with different orientations. For FCC model, when the first local failure happens, it instantly triggers other local failure of joints on circumferential direction and finally forms a spine shape failure pattern on cylinder. But for FLC model, after the first local failure happens, the structure maintains tensile capability until more fracture happens gradually. i.e. small cracks develops on all of the joints of the inclined ribs at the middle of the ring.

6. Buckling analysis

Buckling analysis of cylindrical Fish-Cell metamaterials is beneficial for practical applications of lattice structure with ZPR features in engineering. In this section, buckling characteristics of these structures is studied considering tessellation numbers effect. Numerical analysis for the eigenvalue buckling behaviour of metamaterials uses beam elements to minimize the complexity of the analysis. In these simulations, cylindrical dimensions are fixed while tessellation numbers change; for FCC model tessellation numbers are: 5*3, 10*6, 20*12, 40*24 and 80*48 whereas for FLC model tessellation numbers are: 5*8, 10*16, 20*32 and 40*64. The boundary conditions are fully constrained at one end of the cylinder, while the other end is subjected to 1 N compression force along cylinder axial direction. Moreover, the weight of the metamaterial can be calculated by ABAQUS.

6.1. Buckling modes for FCC and FLC models

Table 3 shows the buckling loads and detailed description of mode shapes for different tessellations of FCC model, where all mode shapes are symmetric in cylindrical coordinate system. The trend of buckling loads show a nonlinear rise as tessellation numbers increase, for instance buckling load for tessellation 80*48 with value 591.56 is 480 times larger than tessellation 5*3 with value of 1.23. This is comparable to weight ratio of 17.2 for these two structures. Therefore, the buckling loads are normalized critical load to weight of each tessellation model for better inception. The trend has also a nonlinear rising behaviour, for example tessellation number 80*48 with the normalized ratio of 574.33 is 30 times larger than tessellation number 5*3 with normalized ratio of 19.10. Moreover, the increment of buckling load for several tessellation numbers is presented in Appendix B.

The buckling mode shape for FCC tessellation 5*3 has a pure bending behaviour for the axis of cylinder with unchanged and not rotated circular cross-section at the middle of cylinder. In contrast, other tessellations do not show bending mode shape at all. The cross-section shape at the middle of the cylinder for tessellation numbers 10*6 and 20*12 are changed to shape of peanut shell, while tessellations 40*24 and

Table 4
Buckling load and mode shapes for Fish-Cells in the Longitudinal Direction of the Cylinder (FLC model).

Tessellation	Eigenvalue	Normalize critical load to weight	Buckling mode shape	Bending of cylinder axis	Cylinder rotation (degree)	Cross section changes at middle
5*8	2.46	14.06	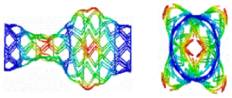	No	0.0034	Irregular shape
10*16	10.97	31.61	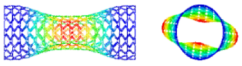	No	0.0261	Oval shape
20*32	38.4	55.57	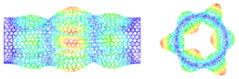	No	0.0174	Tear drop Shape
40*64	139.97	101.43	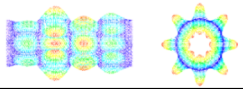	No	0.0036	Four-Pointed Star

80*48 have a three-point star shape and five-point starfish shape. All tessellations except 5*3 have slight torsion in their mode shapes which causes the spiral formation of the cylinder wall. The torsion values measured at the middle of cylinder decrease from 0.064 to 0.019 degree as tessellation numbers increases.

Table 4 shows the buckling loads and detailed description of mode shapes for different tessellations of FLC model, where all mode shapes except tessellation 5*8 are symmetric in cylindrical coordinate system. The trend of buckling loads shows a nonlinear rise as tessellation numbers increase, for instance buckling load for tessellation 40*64 with value 139.97 is almost 57 times larger than tessellation 5*8 with value of 2.46. This is comparable to weight ratio of 7.9 for these two structures. The trend has also a nonlinear rising behaviour, for example tessellation number 40*64 with the normalized critical load to weight ratio of 101.43 is 7.2 times larger than tessellation number 5*8 with normalized ratio of 14.06. The increment trend for buckling load is presented in Appendix B Fig. B1.

Although all FLC tessellations do not show bending mode shape, their cross-section changes to non-circular shapes. For instance, tessellation numbers 5*8 has an irregular shape at the middle of the cylinder. However, the cross-section shape at the middle of the cylinder for FLC models with tessellation numbers 10*16, 20*32 and 40*64 are changed to regular shapes, such as oval, tear drop and four-point star shapes, respectively. All tessellations have very small torsion in their mode shapes with a range of 0.0034 to 0.0261 degree at the middle of the cylinder.

The surface of tessellation number 5*8 has a major bump and indentation at about 25% and 75% of the cylinder length, recalling Fish shape for this mode. However, the surface of tessellation number 10*16 has a major bump and indentation in the same location at the middle of cylinder. Tessellation numbers 20*32 and 40*60 have several humps and depressions on cylinders surface generating chessboard pattern similar to the buckling mode of isogrid cylindrical lattice structures [29,30].

The detailed experimental buckling is an independent research article which might be used to validate these simulation results. However this is beyond the scope of this paper due to complexity, high cost of very time-consuming 3D printing samples and limitation on length of this article. However, the buckling analysis with solid elements for FLC 5*8 and FCC 5*3 are presented in Appendix B, Table B1 to show further support of presented beam results. The mode shapes for both beam models of FCC 5*3 and FLC 5*8 in Table 3 and Table 4 highlight identical behaviour with solid models in Appendix B. The critical buckling loads for solid models of FCC 5*3 and FLC 5*8 are 4.6% and 5.3% higher than those expected by beam models.

Table 5
First Buckling Model and Eigenvalue for Equivalent Shell cylinders.

Buckling mode shape	Eigenvalue Shell cylinder M_{FCC}	Shell cylinder M_{FLC}
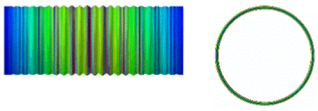	$M_{FCC} = 1631$	$M_{FLC} = 6442.6$

6.2. Buckling comparison of cylindrical Fish-Cell metamaterials and equivalent shell cylinders

Buckling load and mode shapes of cylindrical shells are well studied in literature. The mode shapes of cylindrical shells maybe described as axisymmetric folded rings on the cylinder for isotropic materials as illustrated in Table 5. In this is section the buckling behaviour of two shell cylinders with equivalent mass are compared with buckling performance of cylindrical metamaterials to investigate the effect of Fish-Cells architecture on buckling stiffness.

Two equivalent shell cylinders M_{eq-FCC} for FCC model with tessellation 80*48 and M_{eq-FLC} for FLC model with tessellation 40*64 are analysed with identical mass, boundary conditions and dimensions but with reduced shell thickness. The shell thickness for M_{eq-FCC} and M_{eq-FLC} are 1.2 mm and 0.6 mm respectively. The magnitude of buckling loads for equivalent shell cylinders M_{eq-FCC} and M_{eq-FLC} are1631 N and 6442 N respectively, which are about 2.8 and 46 times greater than FCC and FLC models.

7. Modal analysis

Free vibration study reveals the fundamental vibration characteristics of cylindrical Fish-Cell metamaterial regarding its tessellation numbers and cell directions. Tessellations numbers for models FCC and FLC are set to be the same as those in buckling analysis. Eigenvalue frequency analysis is carried out considering a fixed–fixed boundary condition. Finally, free vibration behaviour of Model FCC with tessellation 80*48 and Model FLC with tessellation 40*64 are compared to equivalent shell cylinders with the identical dimensions and mass but modified density.

Table 6
The first frequency and mode shapes for different tessellations of metamaterial Fish-Cell in Circumferential Direction of the Cylinder (FCC model).

Tessellation	First frequencies (Hz)	First mode shapes	Bending of cylinder axis	Cylinder rotation (degree)	Cross section change
5*3	0.075	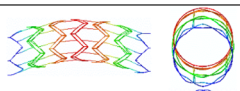	Yes	No	No change
10*6	0.155	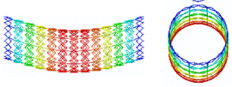	Yes	No	No change
20*12	0.266	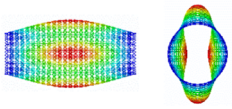	No	0.0022	Peanut shape
40*24	0.377	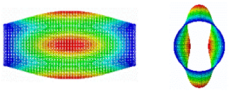	No	0.0014	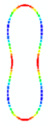 Peanut shape
80*48	0.643	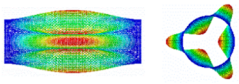	No	0.0005	Three-Pointed star

Table 7
The first frequency and mode shapes for different tessellations of metamaterial Fish-Cells in the Longitudinal Direction of the Cylinder (FLC).

Tessellation	First frequencies (Hz)	First mode shape	Bending of cylinder axis	Cylinder rotation (degree)	Cross section change
5*8	0.065	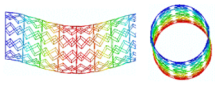	Yes	No	No
10*16	0.085	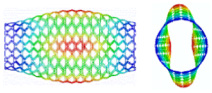	No	No	Peanut
20*32	0.113	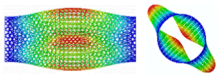	No	No	Peanut
40*64	0.177	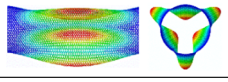	No	No	Three-Pointed star

7.1. Frequency analysis for model FCC and model FLC

Table 6 shows the first frequencies and detailed descriptions of mode shapes for different tessellations of FCC model. The trend of the frequencies shows a nonlinear rise as tessellation numbers increase, for instance frequency for tessellation 80*48 with value 0.64 Hz is 8.3 times larger than tessellation 5*3 with value of 0.075 Hz. The trends of the increment for the frequency show in Appendix C Fig. C1.

The vibration mode shapes for FCC model with tessellation 5*3 and 10*6 have a pure bending behaviour for the axis of cylinder with unchanged and not rotated circular cross-section at the middle of cylinder. In contrast, other tessellations do not show bending mode shape for the axis of cylinder at all. The cross-section shape at the middle of the cylinder for tessellation 20*12 and tessellation 40*24 are changed to shape of a peanut shell, while tessellations 80*48 has a three-point star shape. All tessellations except 5*3 and 10*6 have negligible torsion in their mode shapes with a range of 0.0022 to 0.0005 at the middle of the cylinder.

Table 7 shows the first frequencies and detailed descriptions of mode shapes for different tessellations of FLC model. The trend of frequencies shows a nonlinear rise as tessellation numbers increase. For instance, frequency for tessellation 40*64 with value of 0.177 Hz is almost 2.7 times larger than tessellation 5*8 with value of 0.065 Hz. The frequency trends can be view in Appendix C Table C1. The first vibration mode

Table 8
Comparison of first five frequencies and mode shapes between FCC model (Fish-Cells in the Circumferential direction of the Cylinder) and FLC model (Fish-Cells in Longitudinal direction of the Cylinder) as well as Equivalent Shell Cylinders.

Mode Shape	FCC model Tessellation 80*48			Equivalent Shell Cylinder for FCC model; S_{FCC}		
	Frequency (Hz)	Mode Shape	Cross section change	Frequency (Hz)	Mode Shape	Cross section change
1st &2nd	0.64	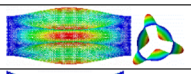		2.05	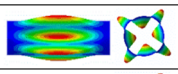	
3rd &4th	0.66	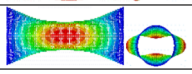		2.50	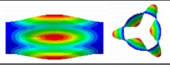	
5th	1.00	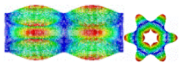		2.53 Hz	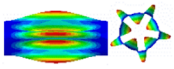	
	FLC model Tessellation 80*48			**Equivalent Shell Cylinder for FCC model; S_{FCC}**		
1st &2nd	0.177	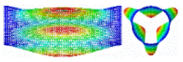		1.99	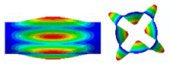	
3rd &4th	0.187	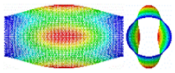		2.32	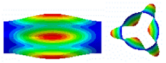	
5th	0.277	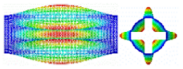		2.54	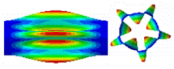	

shapes for FLC model with tessellation 5*8 has a pure bending behaviour on cylinder axis with unchanged circular cross-section at the middle of cylinder. In contrast, other tessellations do not show bending mode shape and their cross-section change to non-circular shapes. For instance, tessellation numbers 10*16 and 20*32 have a peanut shell shape at the middle of the cylinder in compared to three-pointed star shape for tessellation 40*64. All tessellations do not show torsional behaviour in their mode shapes.

Similar to experimental buckling discussion, the detailed experimental modal analysis is an independent research article which might be used to validate these simulation results. However, the modal analysis with solid elements for FLC 5*8 and FCC 5*3 are presented in Appendix C, Table C1 to show further support of presented beam results. The mode shapes for both beam models of FCC 5*3 and FLC 5*8 in Table 6 and Table 7 highlight identical behaviour with solid models in Appendix C. The frequency for solid models of FCC 5*3 and FLC 5*8 are 3.2% and 3.8% higher than those expected by beam models.

7.2. Frequency comparison of cylindrical Fish-Cell metamaterials and equivalent shell cylinders

Table 8 presents the comparison of first, third and fifth frequencies and mode shapes between cylindrical metamaterials and equivalent cylindrical shells to investigate the effect of Fish-Cells architecture on free vibration. It should be mentioned that the second and forth mode shapes and eigenvalues are repetitive for both cylindrical metamaterials and shells. Two equivalent shell cylinders of S_{FCC} for FCC model with tessellation 80*48 and S_{FLC} for FLC model with tessellation 40*64 are analysed with identical dimensions, mass and boundary conditions. However, in order to keep the same mass and dimensions, only the material densities are modified to 559 Kg/m^3 and 281.9 Kg/m^3 for FCC and FLC models.

As demonstrated in Table 8, the first and third frequencies of FCC tessellation 80*48 are very close to each other, i.e. the ratio of these two frequencies are 1.03. However, the fifth frequency increases nonlinearly with the value which is 1.56 times larger than first frequency. Frequencies of equivalent shell S_{FCC} are about 2.5 to 3.8 times larger than FCC metamaterial with similar trend. The first and third frequencies of S_{FCC} are close to each other with ratio of 1.22, whereas the fifth frequency is 1.23 times larger than first frequency. All mode shapes for FCC tessellation 80*48 do not show bending and torsion. The cross-section at the middle of the FCC model for first, third and fifth mode shapes are three-point star, peanut shell shape and a slightly deformed circle.

Although FLC model has a similar trend of frequencies to FCC model; their frequencies are about 3.5 times smaller than FCC metamaterial. The first and third frequencies of FLC tessellation 40*64 are also very close to each other with frequencies ratio of 1.06 as presented in Table 8. The fifth frequency rises nonlinearly with the value which is 1.56 times larger than first frequency very similar to FCC trend. Frequencies of equivalent shell S_{FLC} are about 9 to 12 times larger than FLC metamaterial with similar trend. The first and third frequencies of S_{FLC} are close to each other with ratio of 1.17, whereas the fifth frequency is 1.28 times larger than first frequency. Also, all mode shapes for FLC tessellation 40*64 do not show bending and torsion. Unlike the fifth mode, other mode shapes of both models FCC and FLC are very similar. The cross-section shape at the middle of the FLC model for first, third and fifth mode shapes are three-point star, peanut shell shape and four-pointed star shape.

8. Conclusions

In this paper, novel cylindrical Fish-Cell metamaterials exhibiting zero Poisson's ratio in two different arrangements were introduced for the first time in literature. High-fidelity CAD models were created with the accuracy for at least seven decimal numbers for precise dimensions. Significant number of FEA simulations with fine mesh were performed on high performance computing cluster for different tessellations of both models to investigate the Young's modulus and Poisson's ratio for cylindrical Fish-Cell metamaterial. Finite element simulations with beam elements demonstrated the homogenised behaviour and ideal value of Poison ratio, torsion and Young's modulus for different size ratios and tessellation numbers, while FE models with solid elements demonstrated the reliable deformation mechanisms and stress distribution in more practical cases. The cylindrical models were specifically manufactured using SLS 3D printing technology due to the complexity of the models. Tensile experiments were performed for the validation of Poisson's ratio

Table A1
Dimension of 2D Fish-Cells projected from 3D curved cell for Fish-Cells in the Circumferential direction of Cylinder (FCC) model and Fish-Cell in the Longitudinal direction of Cylinder (FLC) model in FEA simulations and experiments.

Parameter (mm)		*H*	*B*	*b*	*C*	*h*	*t*	*R*	
Simulations	FCC; FLC m = 5 n = 3,6,8,12,16,24,32, 48,64,96,128,192,256, 384,512, 768,1024	192.00	64.00	48.00	16.00	48.00	2.00	model FCC: 152.788	model FLC: 254.648
	FCC; FLC m = 10 n = 6, 12,16, 24,32,48, 64, 96,128, 192,256, 384,512	96.00	32.00	24.00	8.00	24.00	2.00		
	FCC; FLC m = 20 n = 12,24,32, 48,64,96, 192,254, 384	48.00	16.00	12.00	4.00	12.00	2.00		
	FCC; FLC m = 40 n = 24, 64	24.00	8.00	6.00	2.00	6.00	2.00		
	FLC m = 50 n = 80	19.20	12.80	4.80	1.60	4.80	2.00		
	FCC m = 60 n = 36	16.00	5.33	5.33	1.33	4.00	2.00		
Experiments	FCC m = 10 n = 4	24.00	8.00	6.00	2.00	6.00	2.00	38.197	
	FLC m = 5 n = 6	24.00	8.00	6.00	2.00	6.00	2.00	63.622	
Fish Cell	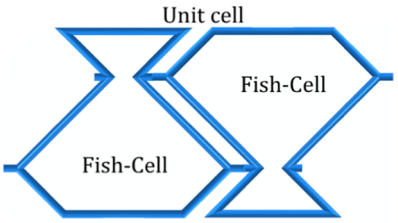								

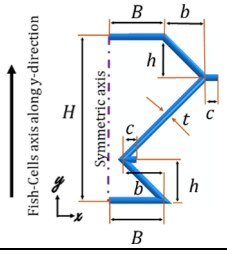

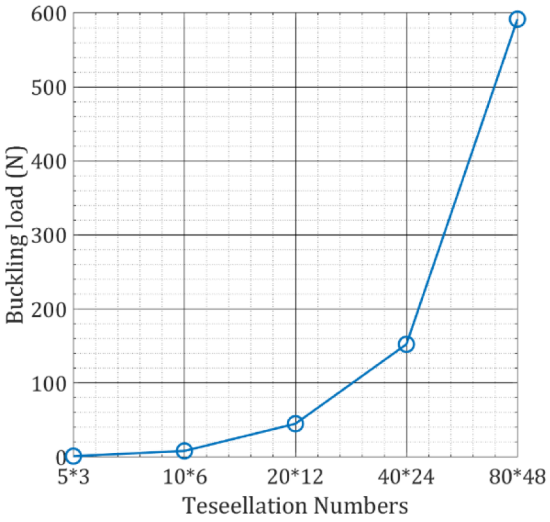

(a)Fish-Cell in the Circumferential Direction of Cylinder (FCC model)

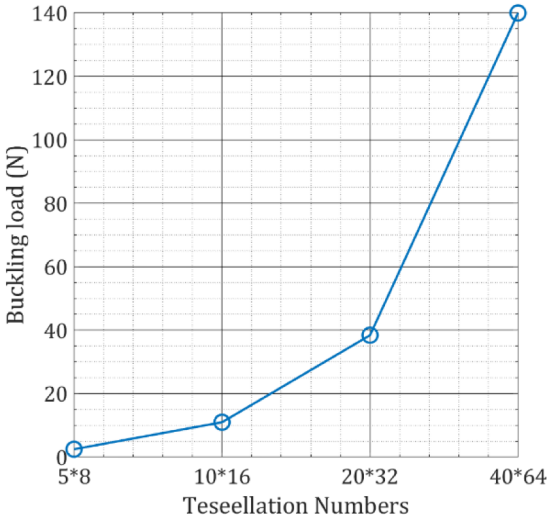

(b)Fish-Cell in the Longitudinal Direction of Cylinder (FLC Model)

Fig. B1. Buckling load for Fish-Cell in the Circumferential Direction of Cylinder (FCC model) and Fish-Cell in the Longitudinal Direction of Cylinder (FLC Model).

and deformation mechanism between experiment and numerical models. The good corelation of results demonstrated the reliability of numerical models for in future optimisation studies. Furthermore, buckling and modal behaviour of the cylindrical Fish-Cells metamaterials were studied and compared with equivalent shell cylinders, highlighting lower range of eigenvalues than equivalent shell cylinder due to the lower stiffness of the metamaterials. Different unit cell orientations and tessellation homogeneity created unique and

Table B1
The critical buckling load and mode shapes of metamaterials with Fish-Cells in the Longitudinal Direction of the Cylinder (FLC) 5*8 and Fish-Cell in Circumferential Direction of the Cylinder (FCC) 5*3.

Model and Tessellation	Critical buckling load(N)	Normalise critical load to weight	Buckling mode shape	Bending of cylinder axis	Cylinder rotation (degree)	Cross section changes at middle
FCC 5*3	1.289	20.32	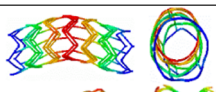	Yes	0	No change
FLC 5*8	2.599	14.97	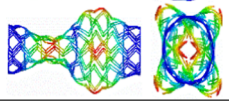	No	0.0036	Irregular shape

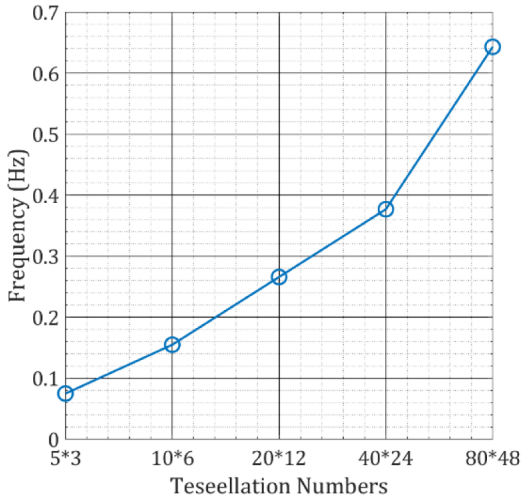

(a)Fish-Cell in the Circumferential Direction of Cylinder (FCC model)

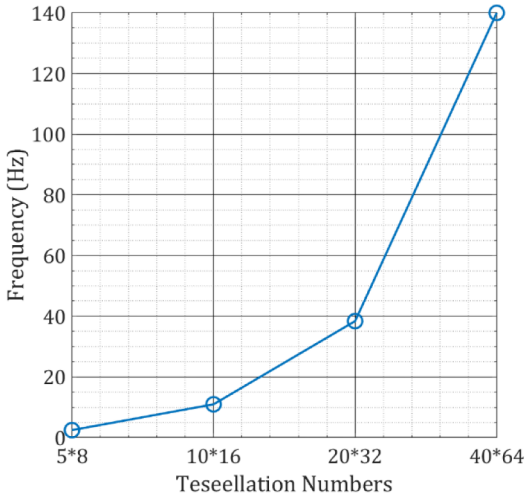

(b)Fish-Cell in the Longitudinal Direction of Cylinder (FLC Model)

Fig. C1. The first frequency for Fish-Cell in the Circumferential Direction of Cylinder (FCC model) and Fish-Cell in the Longitudinal Direction of Cylinder (FLC Model).

Table C1
The first frequency and mode shapes of metamaterials with Fish-Cells in the Longitudinal Direction of the Cylinder (FLC) 5*8 and Fish-Cell in Circumferential Direction of the Cylinder (FCC) 5*3.

Model and Tessellation	First frequencies (Hz)	First mode shape	Bending of cylinder axis	Cylinder rotation (degree)	Cross section change
FLC 5*8	0.0676	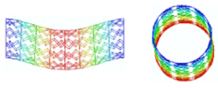	Yes	No	No
FCC 5*3	0.0775	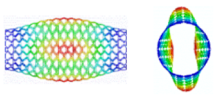	No	No	Peanut

complex buckling and vibration mode shapes due to bending and torsion functions. The results show excellent integration potentials of these metamaterials due to zero Poisson's ratios in cylindrical systems to be used for further realization of advanced medical stents, soft robotics and morphing intake runner of the jet engine.

Declaration of Competing Interest

The authors declare that they have no known competing financial interests or personal relationships that could have appeared to influence the work reported in this paper.

Appendix A

See Table A1.

Appendix B

See Fig. B1 and Table B1.

Appendix C

See Fig. C1 and Table C1.

References

[1] Mohsenizadeh S, Alipour R, Shokri Rad M, Farokhi Nejad A, Ahmad Z. Crashworthiness assessment of auxetic foam-filled tube under quasi-static axial loading. Mater. Des. 2015;88:258–68. https://doi.org/10.1016/j.matdes.2015.08.152.

[2] Xu T, Li G. A shape memory polymer based syntactic foam with negative Poisson's ratio. Mater. Sci. Eng., A 2011;528:6804–11. https://doi.org/10.1016/j.msea.2011.05.034.

[3] Neville RM, Monti A, Hazra K, Scarpa F, Remillat C, Farrow IR. Transverse stiffness and strength of Kirigami zero-ν PEEK honeycombs. Compos. Struct. 2014;114:30–40. https://doi.org/10.1016/j.compstruct.2014.04.001.

[4] Olympio KR, Gandhi F. Zero poisson's ratio cellular honeycombs for flex skins undergoing one-dimensional morphing. J. Intell. Mater. Syst. Struct. 2010;21:1737–53. https://doi.org/10.1177/1045389X09355664.

[5] Gong X, Huang J, Scarpa F, Liu Y, Leng J. Zero Poisson's ratio cellular structure for two-dimensional morphing applications. Compos. Struct. 2015;134:384–92. https://doi.org/10.1016/j.compstruct.2015.08.048.

[6] Mizzi L, Mahdi EM, Titov K, Gatt R, Attard D, Evans KE, et al. Mechanical metamaterials with star-shaped pores exhibiting negative and zero Poisson's ratio. Mater. Des. 2018;146:28–37.

[7] Grima JN, Oliveri L, Attard D, Ellul B, Gatt R, Cicala G, et al. Hexagonal honeycombs with zero Poisson's ratios and enhanced stiffness. Adv. Eng. Mater. 2010;12:855–62. https://doi.org/10.1002/adem.201000140.

[8] Yang H, Ma L. Multi-stable mechanical metamaterials with shape-reconfiguration and zero Poisson's ratio. Mater. Des. 2018;152:181–90. https://doi.org/10.1016/j.matdes.2018.04.064.

[9] Miller TF, Gandhi FS, Rufino RJ. Morphing hull concept for underwater vehicles. Ocean Eng. 2014;92:92–102. https://doi.org/10.1016/j.oceaneng.2014.09.023.

[10] Simons MF, Digumarti KM, Conn AT, Rossiter J. Tiled auxetic cylinders for soft robots. RoboSoft 2019 - 2019 IEEE Int Conf Soft Robot 2019:62–7. https://doi.org/10.1109/ROBOSOFT.2019.8722742.

[11] Haga Y, Muyari Y, Goto S, Matsunaga T, Esashi M. Development of minimally invasive medical tools using laser processing on cylindrical substrates. Electr. Eng. Japan (English Transl. Denki Gakkai Ronbunshi) 2011;176:65–74. https://doi.org/10.1002/eej.21030.

[12] Liu J, Zhang Y. Soft network materials with isotropic negative Poisson's ratios over large strains. Soft Matter 2018;14:693–703. https://doi.org/10.1039/c7sm02052j.

[13] Gao Q, wang Y, Ma Z-D, Zhong H. Analyses on Mechanical Properties of the Cylindrical Double-V Micro-Structure. SAE Tech Pap Ser 2018;1:1–6. https://doi.org/10.4271/2018-01-0118.

[14] Lorato A, Innocenti P, Scarpa F, Alderson A, Alderson KL, Zied KM, et al. The transverse elastic properties of chiral honeycombs. Compos. Sci. Technol. 2010;70(7):1057–63.

[15] Li X, Yang Z, Lu Z. Design 3D metamaterials with compression-induced-twisting characteristics using shear–compression coupling effects. Extrem. Mech. Lett. 2019;29:100471. https://doi.org/10.1016/j.eml.2019.100471.

[16] Wu W, Geng L, Niu Y, Qi D, Cui X, Fang D. Compression twist deformation of novel tetrachiral architected cylindrical tube inspired by towel gourd tendrils. Extrem. Mech. Lett. 2018;20:104–11. https://doi.org/10.1016/j.eml.2018.02.001.

[17] Chen W, Ruan D, Huang X. Optimization for twist chirality of structural materials induced by axial strain. Mater. Today Commun. 2018;15:175–84. https://doi.org/10.1016/j.mtcomm.2018.03.010.

[18] Frenzel T, Kadic M, Wegener M. Supplementary Materials for Three-dimensional mechanical metamaterials with a twist. Science (80-) 2017;358:1027–32. https://doi.org/10.1126/science.aan3456.

[19] Ma C, Lei H, Hua J, Bai Y, Liang J, Fang D. Experimental and simulation investigation of the reversible bi-directional twisting response of tetra-chiral cylindrical shells. Compos. Struct. 2018;203:142–52. https://doi.org/10.1016/j.compstruct.2018.07.013.

[20] Fan HL, Zeng T, Fang DN, Yang W. Mechanics of advanced fiber reinforced lattice composites. Acta Mech Sin Xuebao 2010;26:825–35. https://doi.org/10.1007/s10409-010-0390-z.

[21] Xu Y, Zhang H, Šavija B, Chaves Figueiredo S, Schlangen E. Deformation and fracture of 3D printed disordered lattice materials: Experiments and modeling. Mater. Des. 2019;162:143–53. https://doi.org/10.1016/j.matdes.2018.11.047.

[22] Hao M, Hu Y, Wang B, Liu S. Mechanical behavior of natural fiber-based isogrid lattice cylinder. Compos. Struct. 2017;176:117–23. https://doi.org/10.1016/j.compstruct.2017.05.028.

[23] Vasiliev VV, Barynin VA, Rasin AF. Anisogrid lattice structures - Survey of development and application. Compos. Struct. 2001;54:361–70. https://doi.org/10.1016/S0263-8223(01)00111-8.

[24] Zhang Y, Xue Z, Chen L, Fang D. Deformation and failure mechanisms of lattice cylindrical shells under axial loading. Int. J. Mech. Sci. 2009;51:213–21. https://doi.org/10.1016/j.ijmecsci.2009.01.006.

[25] Nguyen DD, Pham CH. Nonlinear dynamic response and vibration of sandwich composite plates with negative Poisson's ratio in auxetic honeycombs. J. Sandw. Struct. Mater. 2018;20:692–717. https://doi.org/10.1177/1099636216674729.

[26] Cong PH, Long PT, Van Nhat N, Duc ND. Geometrically nonlinear dynamic response of eccentrically stiffened circular cylindrical shells with negative poisson's ratio in auxetic honeycombs core layer. Int. J. Mech. Sci. 2019;152:443–53. https://doi.org/10.1016/j.ijmecsci.2018.12.052.

[27] Li W, Sun F, Wang P, Fan H, Fang D. A novel carbon fiber reinforced lattice truss sandwich cylinder: Fabrication and experiments. Compos. Part A Appl. Sci. Manuf. 2016;81:313–22. https://doi.org/10.1016/j.compositesa.2015.11.034.

[28] Lopatin AV, Morozov EV, Shatov AV. Fundamental frequency of a cantilever composite filament-wound anisogrid lattice cylindrical shell. Compos. Struct. 2015;133:564–75. https://doi.org/10.1016/j.compstruct.2015.07.109.

[29] Naghavi Zadeh M, Dayyani I, Yasaee M. Fish Cells, a new zero Poisson's ratio metamaterial—Part I: Design and experiment. J. Intell. Mater. Syst. Struct. 2020;31:1617–37. https://doi.org/10.1177/1045389X20930079.

[30] Chen Y, Fu MH. Mechanical Properties of a Novel Zero Poisson's Ratio Honeycomb. Adv. Eng. Mater. 2018;20:1–12. https://doi.org/10.1002/adem.201700452.

https://dspace.org/

Structural mechanics of cylindrical fish-cell zero Poisson's ratio metamaterials

Qin, Qing; Dayyani, Iman; Webb, Phil

2022-03-12
Elsevier
https://doi.org/10.1016/j.compstruct.2022.115455
Qin Q, Dayyani I, Webb P. (2022) Structural mechanics of cylindrical fish-cell zero Poisson's ratio metamaterials, Composite Structures, Volume 289, June 2022, Article number 115455

Downloaded from a DSpace repository. https://dspace.org/